On the reduced North Atlantic storminess during the last glacial period: the role of topography in shaping synoptic eddies

Gwendal Riviere, Ségolène Berthou, Guillaume Lapeyre, Masa Kageyama

On the reduced North Atlantic storminess during the last glacial period: the role of topography in shaping synoptic eddies

Gwendal Rivière*

LMD/IPSL, Département de géosciences, ENS, PSL Research University, Ecole Polytechnique, Université Paris Saclay, Sorbonne Universités, UPMC Univ Paris 06, CNRS, Paris, France

Ségolène Berthou

Met Office Hadley Centre, Exeter, United Kingdom

Guillaume Lapeyre

LMD/IPSL, Département de géosciences, ENS, PSL Research University, Ecole Polytechnique, Université Paris Saclay, Sorbonne Universités, UPMC Univ Paris 06, CNRS, Paris, France

Masa Kageyama

LSCE/IPSL, CEA-CNRS-UVSQ, Université Paris Saclay, Gif-sur-Yvette, France

Corresponding author address: LMD-ENS, 24 rue Lhomond, 75005 Paris, France.

E-mail: griviere@lmd.ens.fr

ABSTRACT

The North Atlantic storminess of Last Glacial Maximum (LGM) fully coupled climate simulations is generally less intense than that of their pre-industrial (PI) counterparts, despite having stronger baroclinicity. An explanation for this counterintuitive result is presented by comparing two simulations of the IPSL full climate model forced by PMIP3 (Paleoclimate Modelling Intercomparison Project Phase 3) LGM and PI conditions. Two additional numerical experiments using a simplified dry general circulation model forced by idealized topography and a relaxation in temperature provide guidance for the dynamical interpretation. The forced experiment with idealized Rockies and idealized Laurentide Ice Sheet has a less intense North Atlantic storm-track activity than the forced experiment with idealized Rockies only, despite similar baroclinicity. Both the climate and idealized runs satisfy or support the following statements. The reduced storm-track intensity can be explained by a reduced baroclinic conversion which itself comes from a loss in eddy efficiency to tap the available potential energy as shown by energetic budgets. The eddy heat fluxes are northeastward oriented in the western Atlantic in LGM and are less well aligned with the mean temperature gradient than in PI. The southern slope of the Laurentide Ice Sheet topography forces the eddy geopotential isolines to be zonally oriented at low levels in its proximity. This distorts the tubes of constant eddy geopotential in such a way that they tilt northwestward with height during baroclinic growth in LGM while they are more optimally westward tilted in PI.

1. Introduction

Climate forcing conditions were significantly different during the Last Glacial Maximum (LGM; 21000 yrs ago) compared to the modern climate: orbital parameters were slightly different, greenhouse gas concentrations were lower, and the presence of high and extended ice sheets largely modified the albedo and the Earth's topography (Braconnot et al. 2012; Kageyama et al. 2013a). There are numerous evidences that the ice sheets' topography, especially the Laurentide ice sheet (LIS), accounted for the main changes of the atmospheric circulation and its variability during LGM (Kageyama and Valdes 2000a; Rivière et al. 2010; Pausata et al. 2011; Hofer et al. 2012a,b). LIS altered stationary eddies (Cook and Held 1988; Lofverstrom et al. 2016), synoptic eddies (Kageyama and Valdes 2000a,b; Justino et al. 2005; Laîné et al. 2009) and Rossby wave breaking (Rivière et al. 2010). LIS led to a strong zonal jet (Li and Battisti 2008; Lofverstrom et al. 2014), which is more marked when simulations are forced by the ICE-5G reconstruction of Peltier (2004) (Ullman et al. 2014). It induced a southeastward shift of storm track and increased precipitation in Southern Europe in winter (Hofer et al. 2012a; Beghin et al. 2016).

Several numerical studies have shown that the North Atlantic storm-track eddy activity was less intense during the LGM despite a more intense jet and a stronger baroclinicity in the North Atlantic (Li and Battisti 2008; Laîné et al. 2009; Donohoe and Battisti 2009), even though such a result is not systematic (Merz et al. 2015). Donohoe and Battisti (2009) showed that the smaller-amplitude synoptic eddies seeding the strong baroclinicity in the Western Atlantic explain the weaker Atlantic storm track during the LGM. Laîné et al. (2009) showed that the baroclinic conversion is smaller in LGM runs than in modern-day runs because there is a loss in eddy efficiency to extract energy from the mean flow. First, our study confirms that the reduced storminess during the LGM as detected from recent climate model runs can be attributed to a reduced baroclinic conversion. Second, by

performing numerical simulations with a simplified GCM (General Circulation Model) forced by idealized topography, we show that it is the shaping of the eddies by the topography which makes them less efficient in extracting energy in the region of maximum baroclinicity.

The role played by topography in maintaining storm-track activity is already well-known (Lee and Mak 1996). Because of a high and a low appearing to the northwest and southeast of the mountain center respectively (Ringler and Cook 1997), the baroclinicity generally increases to the southeast of the mountain (Brayshaw et al. 2009). A zonally-localized storm track emerges on the downstream side of the mountains (Inatsu et al. 2002; Cash et al. 2005). However, the exact details of this mechanism strongly depend on the background flow (Son et al. 2009).

The paper systematically compares the results of fully-coupled climate simulations to those of idealized simulations of a dry GCM forced with idealized topography and a relaxation in temperature. Section 2 presents the two types of numerical experiments and the eddy energy budget formulation. Section 3 is dedicated to the results and section 4 provides concluding remarks.

2. Model simulations and methods

a. Coupled climate simulations

The model used for the coupled climate simulations is the Institut Pierre-Simon Laplace Coupled Model, in its IPSL_CM5A_LR version (Dufresne et al. 2013), which is one of the versions used for the CMIP5 exercise in view of the IPCC fifth assessment report. The atmospheric component of the coupled model is LMDZ5A (Hourdin et al. 2013), a grid-point model whose grid has 96 points regularly spaced in longitude, 95 points regularly spaced in latitude (i.e. a resolution of 3.75 degree in longitude and 1.9 degree in latitude) and 39 irregularly spaced vertical levels. Hourdin et al. (2013) presented a complete description of the model and its grid. The ocean component of

IPSL_CM5A_LR is NEMOv3.2 (Madec et al. 1997), at a resolution of 2 degrees refined near the equator and in the Nordic Seas. The sea ice model is LIM2 (Fichefet and Morales-Maqueda 1997, 1999). The land surface scheme is ORCHIDEE (Krinner et al. 2005), which also allows to close the global fresh water budget through the representation of river runoff described in Ngo-Duc et al. (2005, 2007).

We compare two simulations. The first one is the pre-industrial simulation run for CMIP5 (Coupled Model Intercomparison Project Phase 5) (Dufresne et al. 2013). The second one is run with the PMIP3 (Paleoclimate Modelling Intercomparison Project Phase III)-CMIP5 LGM boundary conditions (Braconnot et al. 2011, 2012; Kageyama et al. 2013a). These include lowered atmospheric greenhouse gases (CO_2 at 185 ppm, CH_4 at 350 ppb and N_20 at 200 ppb) and astronomical parameters for 21 ky BP according to Berger (1978), with eccentricity set to 0.018994, obliquity to 22.949 degree and the angle between the vernal equinox and the perihelion on the Earth's trajectory to 180 + 114.42 degrees, with the date of vernal equinox taken as March 21st at noon. The PMIP3 ice sheets (Abe-Ouchi et al. 2015) are imposed: the coastlines are adjusted to the corresponding sea-level drop, which results in more extensive continents, e.g. Bering Strait is closed, the land surface type is modified to an ice sheet surface type over northern North America and Fennoscandia and the elevation is set to the reconstructions globally, the largest difference compared to pre-industrial being over the LGM ice sheets, where they reach several thousand meters (see the orography in Fig. 1f). The LGM simulation is initialised from the pre-industrial simulation and has been run for more than 700 years. Its results are described in Kageyama et al. (2013a,b). Here we use the results from years 600 to 619. At that time, the surface climate is equilibrated. The analysis is made for December-January-February months only and using daily outputs.

b. Idealized GCM simulations

As mentioned in the introduction, there are numerous evidences that the Laurentide Ice Sheet topography is the most important forcing of the glacial climate to explain most of the changes in North Atlantic atmospheric circulation compared to the present climate. Our hypothesis is that it is also this large-scale topography, which affects the North Atlantic storm-track eddy activity. To simply analyze its sole effect we use the dry version of the global primitive-equation spectral model called the Portable University Model of the Atmosphere (PUMA, Fraedrich et al. 2005). It has 10 equally spaced sigma levels and a horizontal resolution of T42 (approximately 2.8°x 2.8°). Rayleigh friction is applied to the two lowest levels with a time scale of about 1 day at $\sigma = 0.9$. An eighth-order hyperdiffusion is used with a damping time scale of 0.1 days. The model is forced by a relaxation in temperature toward the same equilibrium temperature profile and using the same restoration time scales as in Held and Suarez (1994). The model is also forced by an idealized topography in the line of Son et al. (2009) or Gerber and Vallis (2009) with the motivation being here to analyze the effect of the Laurentide Ice Sheet topography in a simple context. The model integration is 6 years and the last 5 years are used for the analysis.

Two different idealized orographies are used: one representing the actual Rockies (grey contours in Fig. 2a) and the other the LGM topography over North America, that is, the Rockies plus the LIS (grey contours in Fig. 2b). The corresponding simulations are hereafter denoted as idPI and idLGM respectively. The mountains' shapes have been analytically prescribed using the hyperbolic tangent function. The maximum height is 3 km for both the idealized Rockies and idealized LIS. Outputs are made every 24 hours as for the analysis of climate runs.

c. Eddy total energy budget

In primitive equations, the time evolution of the eddy total energy $T'_e \equiv \frac{1}{2}(u'^2 + v'^2) + \frac{1}{2S}\theta'^2$ (hereafter denoted as ETE) can be expressed as (Chang et al. 2002; Drouard et al. 2015)

$$\frac{\partial T'_e}{\partial t} = -\nabla \cdot (\mathbf{v} T'_e + \mathbf{v}'_a \Phi') - \frac{1}{S}\theta'(\mathbf{v}' \cdot \nabla \overline{\theta}) - \mathbf{v}' \cdot (\mathbf{v}'_3 \cdot \nabla_3 \overline{\mathbf{v}}) + Res, \tag{1}$$

where $\mathbf{v} = (u, v)$ is the horizontal velocity, $\mathbf{v}_3$ the three-dimensional velocity, θ the potential temperature and $S = -h^{-1}\partial\theta_R/\partial p$ is the static stability with $h = (R/p)(p/p_s)^{R/C_p}$. θ_R is a reference potential temperature, R the gas constant, p_s a reference pressure and C_p the specific heat of air at constant pressure. Overbars and primes indicate the mean flow and deviation from the mean flow respectively. The eddy fields are obtained using a high-pass filter which is a nine-point Welch window applied to daily fields and has a 10-day cutoff period. Compared to the classical 2.5-6 days band-pass filter of Blackmon et al. (1977), the present filter also includes slower time scales between 6 and 10 days to take into account the breaking of synoptic waves (Rivière and Orlanski 2007).

The first three terms on the right hand side (rhs) of Eq. (1) correspond to the energy horizontal flux convergence, baroclinic conversion, and barotropic conversion respectively. The residual term *Res* contains the energy vertical flux convergence whose vertical average is zero and additional terms that are zero when applying a climatological mean (see Eqs (1) and (2) of Drouard et al. 2015, for more details). The residual term also includes dissipation and diabatic generation of ETE.

Following Cai and Mak (1990) and Rivière et al. (2004), the baroclinic conversion that converts the mean available potential energy to eddy potential energy can be written as:

$$-\frac{1}{S}\theta'(\mathbf{v}' \cdot \nabla \overline{\theta}) = \mathbf{F} \cdot \mathbf{B_c}, \tag{2}$$

where the two vectors $\mathbf{F}$ and $\mathbf{B_c}$ are defined by

$$\mathbf{F} \equiv \frac{1}{\sqrt{S}}\theta'(v', -u'), \tag{3}$$

$$\mathbf{B_c} \equiv (\frac{-1}{\sqrt{S}}\frac{\partial\overline{\theta}}{\partial y}, \frac{1}{\sqrt{S}}\frac{\partial\overline{\theta}}{\partial x}). \tag{4}$$

One can also write the baroclinic conversion as

$$\mathbf{F}\cdot\mathbf{B_c} = T_e'|\mathbf{B_c}|E_{ff}, \tag{5}$$

where

$$E_{ff} = \frac{|\mathbf{F}|}{T_e'}\cos(\mathbf{F}, \mathbf{B_c}) \tag{6}$$

with

$$\frac{|\mathbf{F}|}{T_e'} = \frac{\sqrt{\frac{1}{S}\theta'^2(u'^2+v'^2)}}{\frac{1}{2}(u'^2+v'^2)+\frac{1}{2S}\theta'^2}.$$

The baroclinic conversion is thus the product between ETE (T_e'), the baroclinicity amplitude $|\mathbf{B_c}|$ and an eddy efficiency term denoted E_{ff}. The eddy efficiency is itself the product of two terms, $|\mathbf{F}|/T_e'$ and $\cos(\mathbf{F}, \mathbf{B_c})$, which are related to two well-known different notions of instantaneous optimal baroclinic configuration. The cosine of $\mathbf{F}$ and $\mathbf{B_c}$ equals 1 when the two vectors $\mathbf{F}$ and $\mathbf{B_c}$ are collinear, i.e. when the eddy heat fluxes align with the mean temperature gradient. When the temperature gradient is equatorward, the heat fluxes should be poleward for the eddies to efficiently extract energy from the mean flow. And poleward eddy heat fluxes correspond to a westward tilt with height of the eddy geopotential isolines (James 1994). So $\cos(\mathbf{F}, \mathbf{B_c})$ measures the orientation of the tilt with height of the eddy geopotential isolines with respect to the temperature gradient. The ratio $|\mathbf{F}|/T_e'$ estimates the optimal magnitude of the tilt with height of the eddy geopotential isolines. It is maximum and equal to 1 when $\frac{1}{2}(u'^2+v'^2) = \frac{1}{2S}\theta'^2$, that is when the eddy kinetic energy equals the eddy potential energy (see Fig. 1 of Rivière and Joly (2006) for further details). The extraction of energy is thus less efficient when the tilt with height is too strong or too weak.

The baroclinicity $|\mathbf{B_c}|$ is proportional to the Eady growth rate (Lindzen and Farrell 1980; Hoskins and Valdes 1990). It involves the static stability S (hereafter obtained with the climatological mean of θ for each run).

3. Results

Figure 1 presents the climatology of the full climate simulations. The time averages of the anomalous geopotential (defined as the deviation from the zonal mean) at 300 hPa and the anomalous temperature at 500 hPa clearly show a stationary Rossby wave train over North America in both runs, the LGM wave train having higher amplitude than the PI one (Figs. 1a-d). Both wave trains are characterized by a high to the northwest, a low to the northeast and again a high to the southeast of North America (Figs. 1a,b). Anomalies of the LGM and PI wave trains are mostly in phase. Only a slight southeastward shift of the subtropical Atlantic high is noticeable for LGM compared to PI. These features have already been noticed in Lofverstrom et al. (2014) and Merz et al. (2015). The low and high over northeastern America correspond to cold and warm anomalies respectively, whose gradient is associated with a maximum of upper-level zonal wind (Figs. 1a-d) and baroclinicity (Figs. 1e,f). In the North Atlantic, the more intense wave train in LGM creates a stronger upper-level jet, a stronger baroclinicity, but surprisingly, a weaker ETE of about 20% (Figs. 1e,f). This reduction in storm-track eddy activity in LGM is consistent with other recent studies (Li and Battisti 2008; Laîné et al. 2009; Donohoe and Battisti 2009), even though not systematically found (Merz et al. 2015). A more systematic common feature of all these model simulations seems to be a reduction in storminess in the western Atlantic near the Laurentide Ice Sheet but the models behave differently in the central and eastern North Atlantic. In the North Pacific sector, the Pacific jet is more intense in its eastern part and the upper westerlies are stronger over North America between 20°N and 40°N in LGM compared to PI.

The stationary waves for the idealized runs have weaker amplitudes than those of the climate runs (Fig. 2). For idPI, there is a high and a low on the southern and northern parts of the mountain. This north-south dipole orientation is the result of strong nonlinearities (Cook and Held 1992; Ringler and Cook 1997). On the northern part, the anticyclonic anomaly can be partly attributed to the decrease in vorticity as the depth of the fluid diminishes when it flows up the slope. More to the south, the flow being more easily blocked because of the downward slope of the isentropes, there is an increase in vorticity by southward advection of the air (Ringler and Cook 1997). More downstream, near 80°W, the presence of a low and high corresponding to a cold and warm anomaly, reinforces the upper-level jet and the baroclinicity in that region (Figs. 2a,c,e). The downstream anomalies mainly result from a dominant southeastward ray (Cook and Held 1992). Generally speaking, the resulting stationary wave pattern for idPI resembles that obtained in Brayshaw et al. (2009).

The idLGM stationary wave train is similar to the idPI one. There is a slight eastward extension of the high on the northern part of the mountain and the low downstream starts further east near 50°W instead of 90°W for idPI (Fig. 2b). The high to the southeast of the mountain is also slightly more intense. Thus, the two wave trains are similar in amplitude. This is to be contrasted with comprehensive climate model experiments showing that the LIS topography acts to reinforce the stationary waves (e.g., Pausata et al. 2011). The reason why we get similar stationary waves in the two idealized simulations is not clear but may come from our set up as the same restoration temperature is used in both experiments. As a result, the upper-level jet has more or less the same intensity in both simulations. Near 80°W, the cold anomaly to the north is weaker but the warm anomaly to the south is stronger for idLGM than idPI (Figs. 2c,d) which makes the maximum baroclinicity roughly the same in both runs (Figs. 2e,f). However, the storm-track is significantly weaker in intensity for idLGM with a 30 % reduction in ETE. The idealized runs are thus relevant

to investigate why the LIS topography acts to reduce the storm-track eddy activity despite an equivalent baroclinicity.

Figure 3 presents ETE budgets as function of longitudes by averaging Eq. (1) over latitude, pressure and time. In climate runs, the baroclinic conversion has two peaks at the entrance of the Pacific and Atlantic oceanic basins just upstream of the ETE peaks (Figs. 3a,c). As seen in Fig. 3, the energy created by baroclinic conversion is then radiated downstream via energy fluxes (Chang et al. 2002). The barotropic conversion has a small positive peak over North America in a region of confluence (Lee 2000; Rivière 2008), but is generally more negative, especially on the eastern side of the oceanic basins where eddies loose their energy to the mean flow. The main difference between the two simulations in the western Atlantic comes from the baroclinic conversion, which is much greater for PI than LGM. The two other tendency terms do not change much their amplitude compared to the baroclinic conversion. In the eastern Atlantic, the difference changes sign and the LGM baroclinic conversion becomes slightly stronger than its PI counterpart. However, this difference is partly offset by the differences in the other two terms (barotropic conversion rate and energy flux convergence). The less negative barotropic conversion in PI than LGM probably comes from the stronger horizontal shears in LGM, which are directly involved in the barotropic conversion.

The ETE budget of the idealized simulations show similar contributions of the different fluxes west of 60°W (Fig. 3d). However, the idealized storm-tracks extend too far east, which is probably due to the absence of the Eurasian continent, but also to the structure of the stationary waves themselves (Kaspi and Schneider 2013). The stronger ETE for idPI clearly comes from the stronger baroclinic conversion in the entrance region of the storm track (near 60°W), the other two terms present less important differences between idLGM and idPI.

Further insights can be gained by writing the baroclinic conversion as the sum of distinct terms in which $M = |\mathbf{F}|/T'_e$ or $O = \cos(\mathbf{F}, \mathbf{B_c})$ are replaced by constant values:

$$\begin{aligned} < T'_e|\mathbf{B_c}|MO >^{iexp}_{y,z,t} &= < T'_e|\mathbf{B_c}|M >^{iexp}_{y,z,t} < O >^{PI}_{x,y,z,t} + < T'_e|\mathbf{B_c}|O >^{iexp}_{y,z,t} < \mathrm{M} >^{PI}_{x,y,z,t} \\ &+ < T'_e|\mathbf{B_c}| \left(MO - M < O >^{PI}_{x,y,z,t} - < M >^{PI}_{x,y,z,t} O\right) >^{iexp}_{y,z,t} . \end{aligned} \tag{7}$$

The operator $< . >^{iexp}_{y,z,t}$ denotes the average over latitude, height, and time for experiment $iexp = PI$ or LGM. The first term on the rhs of Eq.(7) corresponds to the baroclinic conversion by replacing the orientation of the tilt (O) by its mean value in the PI experiment ($< O >^{PI}_{x,y,z,t}$). The second term corresponds to the baroclinic conversion by replacing the magnitude of the tilt (M) by its mean value in the PI experiment ($< M >^{PI}_{x,y,z,t}$). The third term, called the residual term, involves the correlation between M and O and closes the budget. For both experiments, we stress that we use the same constants $< O >^{PI}_{x,y,z,t}$ and $< M >^{PI}_{x,y,z,t}$ in order to contrast the role of one term against the other when comparing LGM and PI. To get a growth rate, the averaged baroclinic conversion and each term of Eq.(7) are divided by the averaged ETE $< T'_e >^{iexp}_{y,z,t}$.

The result is shown in Fig. 3e and called baroclinic growth rate. Near 60°W, the baroclinic growth rate is smaller for LGM than PI and confirms the key role played by the baroclinic extraction of energy to explain the weaker storm track during LGM. The first term on the rhs of Eq.(7) (magenta lines), which considers changes in both the baroclinicity and tilt magnitude (i.e using the same tilt orientation), is stronger for LGM than PI with almost the same percentage of difference as the baroclinic growth rate computed with only $|\mathbf{B_c}|$ changes ($< T'_e|\mathbf{B_c}| >^{iexp}_{y,z,t} < MO >^{PI}_{x,y,z,t}$, black curves). Therefore, changes in tilt magnitude cannot explain changes in the baroclinic growth rate. In contrast, the second term on the rhs of Eq.(7) (cyan curves), that is the baroclinic growth rate due to both $|\mathbf{B_c}|$ and tilt orientation changes, bring strong similarities with the total baroclinic growth rate. For each run, their variations with longitude are similar and the differences between the two

runs are similar as well. Both terms are much smaller for LGM than PI near their maximum values (i.e 60°W). More downstream in the Atlantic sector, between 20°W and 40°E, the LGM values become slightly greater than their PI counterparts for both terms. Finally, the residual term, that is the third term on the rhs of Eq.(7) (dashed lines), weakly varies with longitude and the difference between the residual terms of the two experiments, despite non negligible, is twice as weak as the difference in the second term on the rhs of Eq.(7) at the entrance of the North Atlantic sector.

To conclude on climate runs, the Atlantic storm track is stronger in PI because baroclinic eddies are more efficient in extracting energy from the mean flow. The stronger baroclinic growth rate in PI comes from the better alignment of $\mathbf{F}$ with $\mathbf{B_c}$, or in other words, from a more optimal tilt orientation. Differences in the tilt magnitude are much smaller. The more optimal tilt orientation in PI with respect to the temperature gradient overwhelms the decrease in baroclinicity.

The conclusions are very similar for idealized runs: the idPI baroclinic growth rate is stronger than the idLGM one in regions of maximum baroclinicity (Fig. 3f), that is in the western Atlantic. In the eastern Atlantic, east of 30°W, the reverse happens, the LGM values are stronger than the PI ones, but this is in a region of weaker baroclinicity and the sector is thus less important as a whole. The stronger PI values in regions of strong baroclinicity explain why the idPI ETE is stronger overall (Fig. 3b). The differences in baroclinic growth rate cannot be explained by the baroclinicity or tilt magnitude differences (black and magenta) but are well captured by the cosine differences (cyan) (Figs. 3h, f). The residual term is almost constant with longitude for each run and the difference between the residual terms of the two runs is small. Therefore, the residual term does not explain the difference in the total baroclinic growth rate. Despite similar baroclinicities, the idPI storm-track is stronger than the idLGM one because of differences in the tilt orientation with the temperature gradient.

Maps of the time-mean eddy efficiency and baroclinic growth rate for the climate runs are shown in Figs. 4a,b. In the region of strong baroclinicity, roughly in the sector limited by (90°W-40°W; 35°N-55°N), E_{ff} is much reduced in LGM compared to PI. It is only half as large as that for PI in the vicinity of the southern slope of the Laurentide ice sheet where the baroclinicity reaches its maximum values. This drastic reduction in eddy efficiency makes the baroclinic growth rate $|\mathbf{B_c}|E_{ff}$ to reach roughly similar peak values in LGM and PI despite the much stronger baroclinicity in LGM. In addition, because high values of $|\mathbf{B_c}|E_{ff}$ cover a smaller area in LGM than in PI, its latitudinal average is smaller in LGM than in PI between 70°W and 30°W (Fig.3e). More downstream, between Greenland and the British Isles, E_{ff} is almost the same between the two runs but, because of higher baroclinicity in LGM than PI in connection with sea ice edge in that region (not shown), the product is a bit stronger in LGM as already seen in Fig. 3c between 30°W and 0°W. In other words, the smaller efficiency in LGM is limited to the Western Atlantic in a region of maximum baroclinicity. The time-mean tilt magnitudes, as measured by $|\mathbf{F}|/T'_e$ (Figs. 4c,d), are spatially homogeneous and are rather similar in the two runs with values around 0.65 found in the mid-latitude regions. In contrast, the time-mean tilt orientation, as measured by $\cos(\mathbf{F}, \mathbf{B_c})$ (Figs. 4e,f), exhibit well-defined regions with high values, in the eastern North America and western North Atlantic, which are more or less the same regions having strong E_{ff}. As for E_{ff}, the LGM $\cos(\mathbf{F}, \mathbf{B_c})$ is more than twice as small as its PI counterpart. Time-mean eddy heat fluxes and temperature gradients are shown in Figs. 4g,h. As the temperature gradient is mainly equatorward in the region of maximum baroclinicity in both runs, the eddy heat fluxes should be poleward to optimally extract energy from the mean flow. Over the southern slope of the Laurentide ice sheet, that is north of 40°N, the LGM heat fluxes are mainly northeastward oriented whereas the PI heat fluxes are purely northward oriented in that sector. This confirms the fact that, in the vicinity of

the southern slope of the Laurentide ice sheet, vectors $\mathbf{F}$ and $\mathbf{B_c}$ do not align with each other in the LGM run and largely explains the reduction in eddy efficiency in that sector for that run.

The idealized simulations show a similar picture. E_{ff} is 20% stronger in idPI than idLGM on the immediate downstream side of the idealized Rocky mountains, that is between 100°W and 40°W and south of 50°N, in the region of maximum baroclinicity (Figs. 5a,b). Since the baroclinicity is roughly the same in the two runs, the baroclinic growth rate $E_{ff}|\mathbf{B_c}|$ is also stronger in idPI. More downstream, between 20°W and 20°E, E_{ff} is smaller in idPI but, as the baroclinicity is less strong there, it is not a key sector to have an important impact on the growth of baroclinic eddies as a whole. Therefore, it is the region closer to the mountains which makes the difference between the idPI and idLGM storm-track intensities due to a loss in eddy efficiency there. The analysis of the separated magnitude and orientation of the tilt shows that the reduction in E_{ff} in LGM is mostly due to the tilt orientation and much less to the tilt magnitude. As for the climate runs, the idLGM eddy heat fluxes are mainly northeastward oriented along the southern slope of the idealized Laurentide topography near 50°N (Fig. 5h) while they mostly point toward the north in idPI. This reveals that the eddy geopotential isolines tilt westward with height almost everywhere in idPI whereas they tilt northwestward with height near the idealized Laurentide topography in idLGM.

To get further insights on the reasons of this change in the orientation of the eddy heat fluxes near the Laurentide ice sheet, regression maps are shown from Figs. 6 to 11. The regression is made on the value of the high-pass geopotential height at a reference point (60°W, 45°N), which is chosen to be within the region of maximum baroclinicity. The regressed geopotential, temperature and wind components are used to compute the eddy heat fluxes and eddy efficiency. Let us first discuss the climate runs (Figs. 6-8). Classical baroclinic wave structures are visible in the regressed eddy geopotential heights in Figs. 6a,b. At upper levels, there is no drastic difference between LGM and

PI, except for the low near 30°W which is much more elongated in PI (Figs. 6a,b). To estimate the anisotropic structure of the baroclinic eddies, we have computed the ratio between the meridional and zonal extents of the contour representing 50% of the extrema of Z'. For the strongest high (low), the ratio is about 1.1 (1.6) for LGM and 1.2 (2.2) for PI. Even though the high is only slightly more elongated in PI than LGM, this feature was systematically found when changing the reference grid points.

Larger differences are visible at 800 hPa between the two regressions. Extrema of the 800-hPa high-pass geopotential height are located further south in LGM compared to PI (Figs. 6a,b and 7a,b). This can be explained by the presence of the Laurentide ice sheet, which imposes the lower-level perturbation to be located south of it. Furthermore, in LGM, the 800-hPa eddy geopotential isolines and associated winds are parallel to the mountain isoheights north of the low between 90°W and 65°W and north of the high between 60°W and 50°W (Fig. 7b). The ratio between the meridional and zonal extents of the low-level high is 1.1 for LGM and 1.4 for PI confirming the less meridionally stretched eddy for the former run. In between the low and high anomalies, the winds point northwestward but the cross-section in that sector shows that the meridional wind decreases rapidly toward zero closer to the mountain in LGM (Fig. 7d). So the southern slope of the Laurentide ice sheet can be considered as a zonally-oriented wall along which the horizontal winds should be mainly zonal to satisfy the free-slip boundary condition. It is clear that in the PI simulation (Figs. 7a,c), lower-level meridional winds can reach larger values over the entire latitudinal band between 35°and 55°N.

As for the time-mean values, the eddy efficiency E_{ff} deduced from regressed fields is stronger in PI than LGM from 100°W to 40°W. More downstream, in the eastern Atlantic, they have similar values (Figs. 6c-e). Consistently, the cosine between $\mathbf{F}$ and $\mathbf{B_c}$ is generally stronger between 100°W and 40°W in PI (Figs. 8a,b): for instance, there are stronger positive values between 80°W

and 60°W leading to stronger E_{ff} values there (Fig. 6e), and the area covered by negative values is smaller in PI as well, which also appears in E_{ff} values. The eddy heat fluxes (Figs. 8c,d) are more poleward oriented in PI run as a whole: first, regions of equatorward oriented heat fluxes (white regions) are larger in LGM than PI and second, in regions where the fluxes have a positive poleward component, they are also eastward oriented (see e.g., the area near Newfoundland north of 45°N between 70°W and 55°W), consistent with the time mean eddy heat fluxes of Fig. 4h. Vector **F** is plotted in Figs. 8e,f, together with the 20-m contour of the eddy geopotential height at different levels. **F**, which is perpendicular to the eddy heat fluxes, is useful to indicate the local orientation of the tilt with height of the geopotential isolines. By construction, it is perpendicular to the geopotential contours and points toward geopotential extrema at low levels. Over the southern slope of the Laurentide ice sheet, **F** is southeastward oriented and the eddy geopotential isolines tilt northwestward with height in LGM (Fig. 8f). The presence of the ice sheet imposes eddy geopotential extrema at lower levels to be located more southward, it distorts the tubes of constant eddy geopotential in such a way that they tilt northwestward with height. In contrast, in PI, there is no such constraint, **F** is more eastward oriented and the eddy geopotential isolines have a clearer westward tilt with height (Fig. 8e).

The main differences found in the regression maps of the two climate runs are also seen in those of the idealized experiments. Although the baroclinic eddies have more or less the same shape at upper levels (Figs. 9a,b), they are significantly less meridionally stretched at lower levels in idLGM compared to idPI in the vicinity of the Laurentide Ice Sheet (differences in the ratio between the meridional and zonal extents vary between 10% and 30%). In addition to the more zonally-oriented eddy geopotential isolines and winds over the southern slope of the ice sheet, extrema of 800-hPa eddy geopotential are found further south in idLGM (Figs. 9a,b and 10a,b). In between the low and high anomalies, the meridional wind approaches zero closer to the ice sheet

(Figs. 10c,d). The eddy efficiency reaches stronger positive values and smaller negative values in idPI than idLGM between 100°W and 40°W, that is, close to the idealized ice sheet (Figs. 9c-e). This comes from the difference in the cosine between $\mathbf{F}$ and $\mathbf{B_c}$ (Figs. 11a,b). The poleward (equatorward) eddy heat fluxes cover smaller (larger) areas in idLGM than idPI (Fig. 11c,d) and the eddy heat fluxes are mainly eastward oriented over the idealized ice sheet slope in idLGM (Figs. 11c,d). The $\mathbf{F}$ vector is more southeastward oriented in idLGM over the topography while it is more purely eastward oriented in idPI (Figs. 11e,f). This is consistent with the pronounced northwestward tilt with height of the eddy geopotential isolines in idLGM and the dominance of the westward tilt with height in idPI (Figs. 11e,f). Finally, the regions of eastward tilt with height are larger in idLGM than idPI. The latter characteristic is more difficult to interpret from the direct constraint imposed by the ice sheet but probably comes together with the distortion of the tubes of constant eddy geopotential by the topography.

4. Conclusion and discussion

The present study is summarized as follows. The North Atlantic storminess is reduced in the LGM compared to PI conditions both in a full climate model and in an idealized model forced by LGM or present-day orographies. This is in apparent contradiction with a baroclinicity of similar or even larger amplitude in LGM than PI runs.

In both climate and idealized runs, an energetic budget shows that the reduced storm-track intensity can be explained by a reduced baroclinic conversion which itself results from a loss in eddy efficiency to tap the available potential energy. The eddies are less efficient in LGM because their geopotential isolines tilt northwestward with height near the baroclinicity maximum south of the Laurentide ice sheet. It means that the eddy heat fluxes point northeastward and are less well collinear with the north-south oriented temperature gradient than in PI where the eddy heat

fluxes are more purely northward oriented. The northwestward tilt with height of the geopotential isolines in LGM is shown to be related to the mechanical constraint exerted by the southern slope of the Laurentide ice sheet: the ice sheet plays the role of a zonally-oriented wall which forces the winds to be zonal in its proximity and lower-level eddy geopotential extrema are always located further south of the ice sheet. Therefore, when an upper-level wave approaches the baroclinic zone near the ice sheet, it will necessarily form lower-level perturbation further south and the eddy geopotential isolines will tend to northwestward tilt with height during baroclinic growth. In other words, the presence of the ice sheet distort the tubes of constant eddy geopotential in such a way that baroclinic eddies are less efficient in extracting the available mean potential energy.

The paper illustrates how large-scale mountains can shape baroclinic eddies and affect baroclinic conversion rates in such a way that the downstream storminess is reduced. A similar reduction has been shown by Park et al. (2010) to explain the midwinter suppression of the North Pacific storminess but their underlying mechanism differs from ours as it is mainly based on a change in the orientation of wave propagation.

One might invoke the barotropic governor mechanism proposed by James (1987) to explain the loss of eddy efficiency in extracting potential energy at LGM. Indeed, as the jet is narrower in LGM climate run and its lateral shears stronger (twice as large as in PI; see Figs. 1c,d), this would tend to reduce the ability of baroclinic eddies to extract energy. Although we cannot discard the barotropic governor mechanism hypothesis in the climate runs, we note that the strongest reduction in eddy efficiency appears in the immediate vicinity of the southern slope of the Laurentide Ice Sheet (Fig. 4), which strongly suggests that the mechanism proposed in the present paper is at play. In the idealized experiments, lateral shears have almost the same amplitude (see the zonal wind in Figs. 2c,d) and the barotropic governor mechanism is unlikely to occur.

Donohoe and Battisti (2009) showed that the main mechanism explaining the reduction of the North Atlantic storminess at LGM w.r.t. PI was the reduced seeding from the Pacific, due to the presence of the ice sheet, together with a stabilizing effect of the three-dimensional jet structure. They first performed a linear stability analysis which shows that the LGM jet is more unstable than the PI jet, even though the difference in the linear growth rate is smaller than the difference in the Eady growth rate. Their stability analysis considered the unique effect of the LGM characteristics onto the jet but did not include the direct topographic effect on baroclinic eddies. Our approach further includes the direct effect of the topography on baroclinic eddies and shows that it has a stabilising influence. Donohoe and Battisti (2009) also showed that the LGM storms grow more rapidly in the North Atlantic than PI storms and the difference between their two climate runs relies on the stronger upstream seeding in PI. They found more intense and more frequent upper-level precursors coming from the Pacific in PI run. This is probably an effect which is also present in our climate runs as the eddy total energy is stronger in PI than LGM in the eastern North Pacific and over North America (see Figs. 1e,f and 3a). However, the two idealized runs show similar intensities in eddy total energy just upstream of the idealized Rockies. So upstream seeding is unlikely to explain the difference between the two idealized runs. Donohoe and Battisti (2009) did not explain the reasons for the stronger upstream seeding of waves coming from the Pacific in PI but this would be important to analyze in the future. Our climate runs provide some information about it. They show that in the eastern Pacific a significant difference in ETE between PI and LGM appears near 120°W-100°W (Fig. 3a). The difference comes from both the baroclinic and barotropic conversion terms (Fig. 3c). The stronger baroclinic conversion in PI obviously results from the tilt orientation (Fig. 3e). The reduction in eddy efficiency at 140°W is strong near the western boundary of the Laurentide ice sheet (Figs. 4a,b,e,f). A similar reasoning to what was shown in the present paper for the western Atlantic can be done in that sector too and is supported

by regression maps (not shown). The stronger barotropic sink in the eastern Pacific in LGM can be partly attributed to the stronger shears seen there (Fig. 1). Further analysis of the Pacific storm track in various LGM and PI runs would be necessary to provide a deeper understanding of Northern Hemisphere storm-track eddy activity in LGM as a whole.

References

Abe-Ouchi, A., and Coauthors, 2015: Ice-sheet configuration in the CMIP5/PMIP3 Last Glacial Maximum experiments. *Geosci. Model Dev.*, **8**, 3621–3637.

Beghin, P., S. Charbit, M. Kageyama, N. Combourieu-Nebout, C. Hatté, C. Dumas, and J. Peterschmitt, 2016: What drives LGM precipitation over the western Mediterranean? A study focused on the Iberian Peninsula and northern Morocco. *Clim. Dyn.*, **46**, 2611–2631.

Berger, A. L., 1978: Long-term variations of daily insolation and quaternary climatic changes. *J. Atmos. Sci.*, **35**, 2362–2367.

Blackmon, M., J. Wallace, N. Lau, and S. Mullen, 1977: An observational study of the northern hemisphere wintertime circulation. *J. Atmos. Sci.*, **34**, 1040–1053.

Braconnot, P., S. P. Harrison, M. Kageyama, P. J. Bartlein, V. Masson-Delmotte, A. Abe-Ouchi, B. Otto-Bliesner, and Y. Zhao, 2012: Evaluation of climate models using palaeoclimatic data. *Nat. Clim. Change*, **2**, 417–424.

Braconnot, P., S. P. Harrison, B. Otto-Bliesner, A. Abe-Ouchi, J. Jungclaus, and J.-Y. Peterschmitt, 2011: The Paleoclimate Modeling Intercomparison Project contribution to CMIP5. *CLIVAR Exchanges*, **16**, 15–19.

Brayshaw, D. J., B. J. Hoskins, and M. Blackburn, 2009: The basic ingredients of the North Atlantic storm track. Part I: land-sea contrast and orography. *J. Atmos. Sci.*, **66**, 2539–2558.

Cai, M., and M. Mak, 1990: On the basic dynamics of regional cyclogenesis. *J. Atmos. Sci.*, **47**, 1417–1442.

Cash, B. A., P. J. Kushner, and G. K. Vallis, 2005: Zonal asymmetries, teleconnections, and annular patterns in a GCM. *J. Atmos. Sci.*, **62**, 207–219.

Chang, E. K. M., S. Lee, and K. Swanson, 2002: Storm track dynamics. *J. Climate*, **15**, 2163–2183.

Cook, K. H., and I. M. Held, 1988: Stationary waves of the Ice Age climate. *J. Climate*, **1**, 807–819.

Cook, K. H., and I. M. Held, 1992: The stationary response to large-scale orography in a general circulation model and a linear model. *J. Atmos. Sci.*, **49**, 525–539.

Donohoe, A., and D. S. Battisti, 2009: Causes of reduced North Atlantic storm activity in a CAM3 simulation of the Last Glacial Maximum. *J. Climate*, **22**, 4793–4808.

Drouard, M., G. Rivière, and P. Arbogast, 2015: The link between the North Pacific climate variability and the North Atlantic Oscillation via downstream propagation of synoptic waves. *J. Climate*, **28**, 3957–3976.

Dufresne, J.-L., and Coauthors, 2013: Climate change projections using the IPSL-CM5 Earth System Model: from CMIP3 to CMIP5. *Clim. Dyn.*, **40**, 2123–2165.

Fichefet, T., and A. M. Morales-Maqueda, 1997: Sensitivity of a global sea ice model to the treatment of ice thermodynamics and dynamics. *J. Geophys. Res.*, **102**, 12 609–12 646.

Fichefet, T., and A. M. Morales-Maqueda, 1999: Modelling the influence of snow accumulation and snowice formation on the seasonal cycle of the antarctic seaice cover. *Clim. Dyn.*, **15**, 251–268.

485 Fraedrich, K., E. Kirk, U. Luksh, and F. Lunkeit, 2005: The Portable University Model of the
486 Atmosphere (PUMA): Storm track dynamics and low-frequency variability. *Meteor. Z.*, **14 (6)**,
487 735–745.

488 Gerber, E. P., and G. K. Vallis, 2009: On the zonal structure of the North Atlantic Oscillation and
489 Annular Modes. *J. Atmos. Sci.*, **66**, 332–352.

490 Held, I. M., and M. J. Suarez, 1994: A proposal for the intercomparison of the dynamical cores of
491 atmospheric general circulation models. *Bull. Amer. Meteor. Soc.*, **75**, 1825–1830.

492 Hofer, D., C. C. Raible, A. Dehnert, and J. Kuhlemann, 2012a: The impact of different glacial
493 boundary conditions on atmospheric dynamics and precipitation in the North Atlantic region.
494 *Clim. Past*, **8**, 935–949.

495 Hofer, D., C. C. Raible, N. Merz, A. Dehnert, and J. Kuhlemann, 2012b: Simulated winter circu-
496 lation types in the North Atlantic and European region for preindustrial and glacial conditions.
497 *Geophys. Res. Lett.*, **39**, L15 805.

498 Hoskins, B. J., and P. J. Valdes, 1990: On the existence of storm-tracks. *J. Atmos. Sci.*, **47**, 1854–
499 1864.

500 Hourdin, F., and Coauthors, 2013: Impact of the LMDZ atmospheric grid configuration on the
501 climate and sensitivity of the IPSL-CM5A coupled model. *Clim. Dyn.*, **40**, 2167–2192.

502 Inatsu, M., H. Mukougawa, and S.-P. Xie, 2002: Stationary eddy response to surface boundary
503 forcing: Idealized GCM experiments. *J. Atmos. Sci.*, **59**, 1898–1915.

504 James, I. N., 1987: Suppression of baroclinic instability in horizontally sheared flows. *J. Atmos.*
505 *Sci.*, **44**, 3710–3720.

James, I. N., 1994: *Introduction to circulating atmospheres*. Cambridge University Press, 422 p.

Justino, F., A. Timmermann, U. Merkel, and E. P. Souza, 2005: Synoptic reorganization of atmospheric flow during the Last Glacial Maximum. *J. Climate*, **18**, 2826–2846.

Kageyama, M., and P. J. Valdes, 2000a: Impact of the North American ice-sheet orography on the Last Glacial Maximum eddies and snowfall. *Geophys. Res. Lett.*, **27**, 1515–1518.

Kageyama, M., and P. J. Valdes, 2000b: Synoptic-scale perturbations in AGCM simulations of the present and Last Glacial Maximum climates. *Clim. Dyn.*, **16**, 517–533.

Kageyama, M., and Coauthors, 2013a: Mid-Holocene and Last Glacial Maximum climate simulations with the IPSL model: part I: comparing IPSL-CM5A to IPSL-CM4. *Clim. Dyn.*, **40**, 2447–2468.

Kageyama, M., and Coauthors, 2013b: Mid-Holocene and Last Glacial Maximum climate simulations with the IPSL model: part II: model-data comparisons. *Clim. Dyn.*, **40**, 2469–2495.

Kaspi, Y., and T. Schneider, 2013: The role of stationary eddies in shaping midlatitude storm tracks. *J. Atmos. Sci.*, **70**, 2596–2613.

Krinner, G., and Coauthors, 2005: A dynamic global vegetation model for studies of the coupled atmosphere-biosphere system. *Global Biogeochem. Cycles*, **19**, GB1015.

Laîné, A., and Coauthors, 2009: Northern hemisphere storm tracks during the last glacial maximum in the PMIP2 ocean-atmosphere coupled models: energetic study, seasonal cycle, precipitation. *Clim. Dyn.*, **32**, 593–614.

Lee, S., 2000: Barotropic effects on atmospheric storm-tracks. *J. Atmos. Sci.*, **57**, 1420–1435.

Lee, W.-J., and M. Mak, 1996: The role of orography in the dynamics of storm tracks. *J. Atmos. Sci.*, **53**, 1737–1750.

Li, C., and D. S. Battisti, 2008: Reduced Atlantic storminess during Last Glacial Maximum: Evidence from a coupled climate model. *J. Climate*, **21**, 3561–3579.

Lindzen, R. S., and B. Farrell, 1980: A simple approximate result for the maximum growth rate of baroclinic instabilities. *J. Atmos. Sci.*, **37**, 1648–1654.

Lofverstrom, M., R. Caballero, J. Nilsson, and J. Kleman, 2014: Evolution of the large-scale atmospheric circulation in response to changing ice sheets over the last glacial cycle. *Clim. Past.*, **10**, 1453–1471.

Lofverstrom, M., R. Caballero, J. Nilsson, and G. Messori, 2016: Stationary wave reflection as a mechanism for zonalizing the Atlantic winter jet at the LGM. *J. Atmos. Sci.*, **73**, 3329–3342.

Madec, G., P. Delecluse, M. Imbard, and C. Levy, 1997: OPA version 8.1 ocean general circulation model reference manual. Tech. rep., 3. Tech. rep. LODYC, 91pp pp.

Merz, N., C. C. Raible, and T. Woollings, 2015: North Atlantic eddy-driven jet in interglacial and glacial winter climates. *J. Climate*, **28**, 3977–3997.

Ngo-Duc, T., K. Laval, J. Polcher, A. Lombard, and A. Cazenave, 2005: Effects of land water storage on global mean sea level over the past half century. *Geophys. Res. Lett.*, **32**, L09 704.

Ngo-Duc, T., K. Laval, G. Ramillien, J. Polcher, and A. Cazenave, 2007: Validation of the land water storage simulated by Organising Carbon and Hydrology in Dynamic Ecosystems (ORCHIDEE) with Gravity Recovery and Climate Experiment (GRACE) data. *Water Resour Res*, **43**, W04 427.

547 Park, H.-S., J. C. H. Chang, and S.-W. Son, 2010: The role of the Central Asian mountains on the
548 midwinter suppression of North Pacific storminess. *J. Atmos. Sci.*, **67**, 3706–3720.

549 Pausata, F. S. R., C. Li, J. J. Wettstein, M. Kageyama, and K. H. Nisancioglu, 2011: The key role
550 of topography in altering North Atlantic atmospheric circulation during the last glacial period.
551 *Clim. Past*, **7**, 1089–1101.

552 Peltier, W. R., 2004: Global glacial isostasy and the surface of the ice-age Earth: The ICE-5G
553 (VM2) model and GRACE. *Ann. Rev. Earth Planet. Sci.*, **32**, 111–149.

554 Ringler, T. D., and K. H. Cook, 1997: Factors controlling nonlinearity in mechanically forced
555 stationary waves over orography. *J. Atmos. Sci.*, **54**, 2612–2629.

556 Rivière, G., 2008: Barotropic regeneration of upper-level synoptic disturbances in different con-
557 figurations of the zonal weather regime. *J. Atmos. Sci.*, **65**, 3159–3178.

558 Rivière, G., B. L. Hua, and P. Klein, 2004: Perturbation growth in terms of baroclinic alignment
559 properties. *Quart. J. Roy. Meteor. Soc.*, **130**, 1655–1673.

560 Rivière, G., and A. Joly, 2006: Role of the low-frequency deformation field on the explosive
561 growth of extratropical cyclones at the jet exit. Part II: baroclinic critical region. *J. Atmos. Sci.*,
562 **63**, 1982–1995.

563 Rivière, G., A. Laîné, G. Lapeyre, D. Salas-Mélia, and M. Kageyama, 2010: Links between
564 Rossby wave breaking and the North Atlantic Oscillation - Arctic Oscillation in present-day
565 and Last Glacial Maximum climate simulations. *J. Climate*, **23**, 2987–3008.

566 Rivière, G., and I. Orlanski, 2007: Characteristics of the Atlantic storm-track eddy activity and its
567 relation with the North Atlantic Oscillation. *J. Atmos. Sci.*, **64**, 241–266.

568 Son, S.-W., M. Ting, and L. M. Polvani, 2009: The effect of topography on storm-track intensity
569 in a relatively simple general circulation model. *J. Atmos. Sci.*, **66**, 393–411.

570 Ullman, D. J., A. N. LeGrande, A. E. Carlson, F. S. Anslow, and J. M. Licciardi, 2014: Assessing
571 the impact of Laurentide Ice Sheet topography on glacial climate. *Clim. Past.*, **10**, 487–507.

LIST OF FIGURES

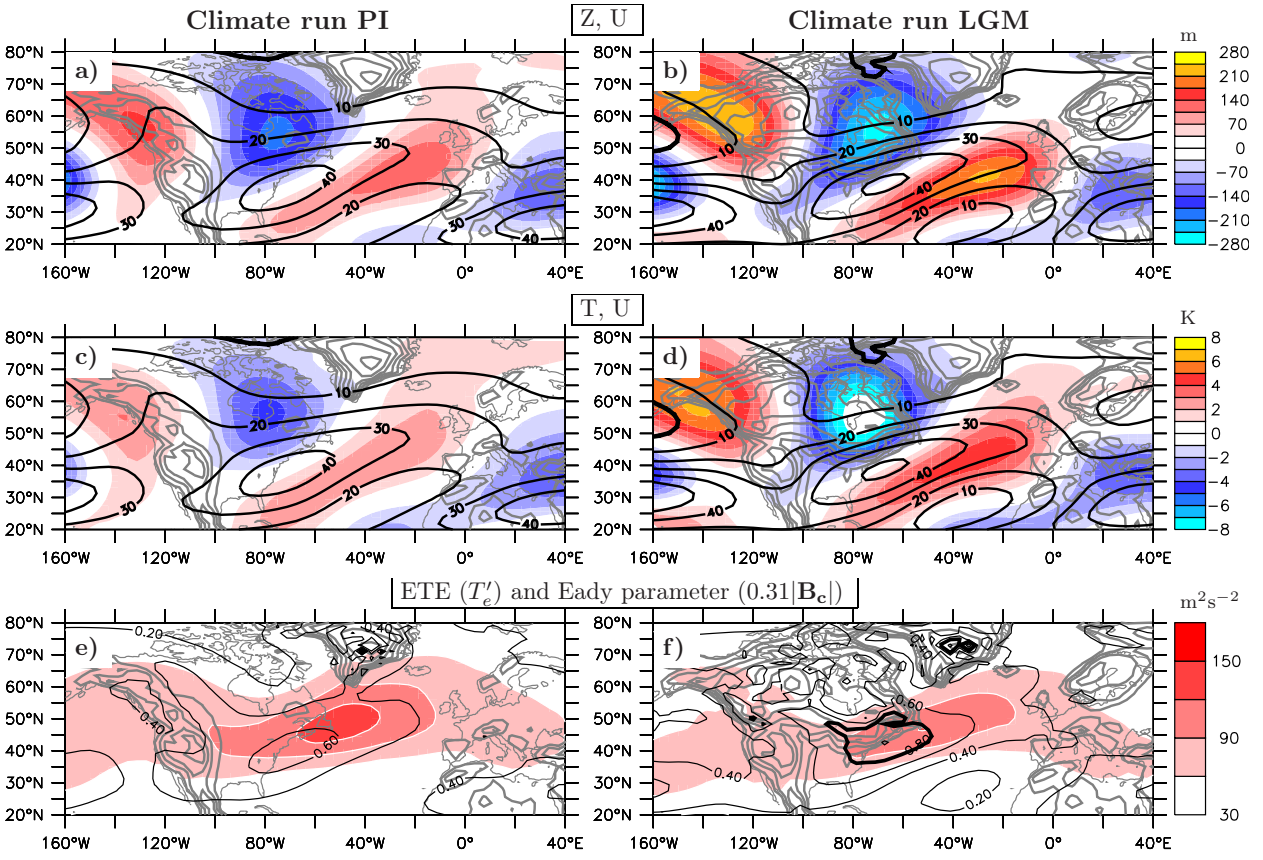

FIG. 1. (a), (b) Climatology of the anomalous (deviation from the zonal mean) geopotential height (shadings; int: 35 m) and the zonal wind at 300 hPa (contours; int: 10 m s^{-1} for positive values only and the zero line is in bold); (c), (d) Climatology of the anomalous (deviation from the zonal mean) temperature at 500 hPa (shadings; int: 1 K) and the zonal wind at 300 hPa (contours; int: 10 m s^{-1} for positive values only and the zero line is in bold); (e), (f) Eady growth rate $0.31|\mathbf{B_c}|$ (contours; int 0.2 day^{-1} with 0.8 day^{-1} in thick contour) and high-pass eddy total energy averaged between 250 and 850 hPa (shadings; int: 30 m^2 s^{-2}). (Left column) PI and (right column) LGM simulations. Grey contours correspond to the height of the orography (int: 500 m, starting from 500m).

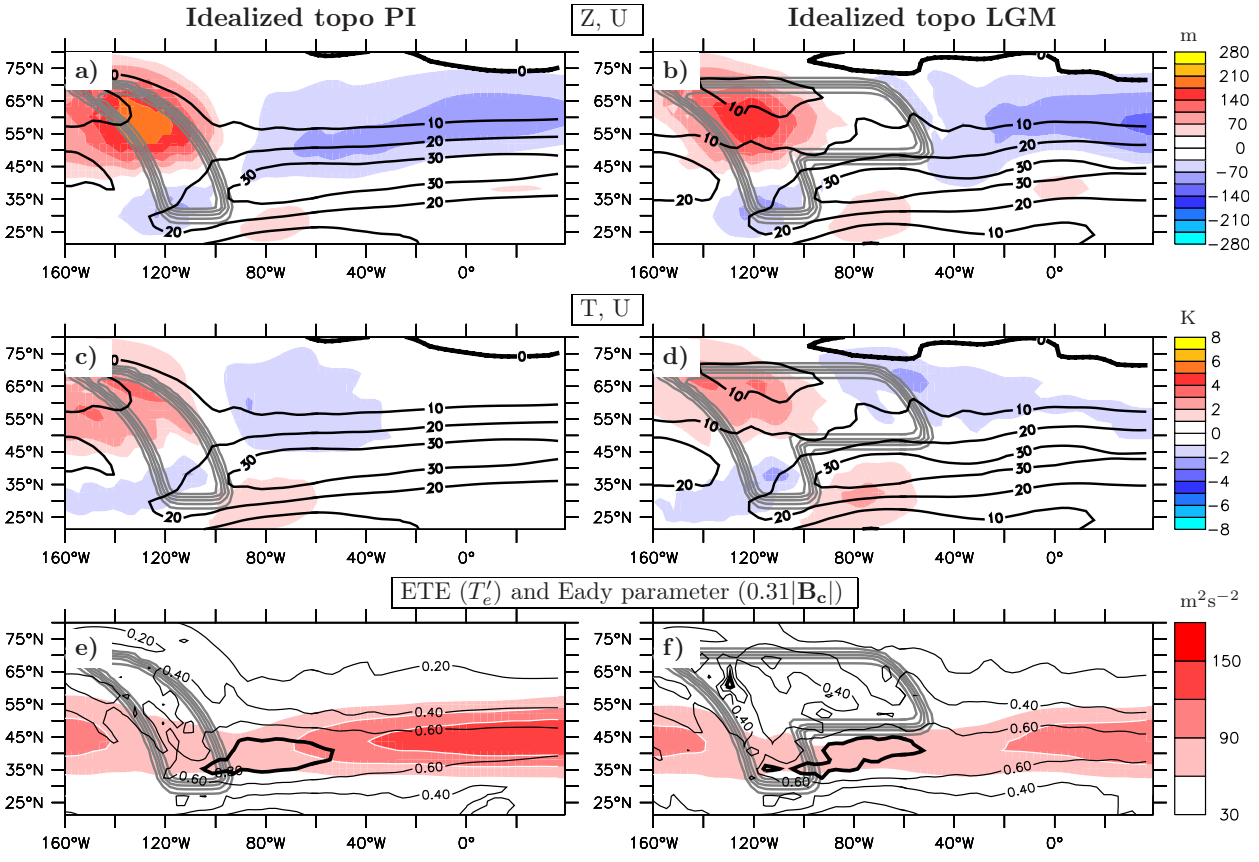

634 FIG. 2. As in Fig. 1 but for the simulations forced with (left) idealized Rockies (right) idealized LGM topog-
635 raphy.

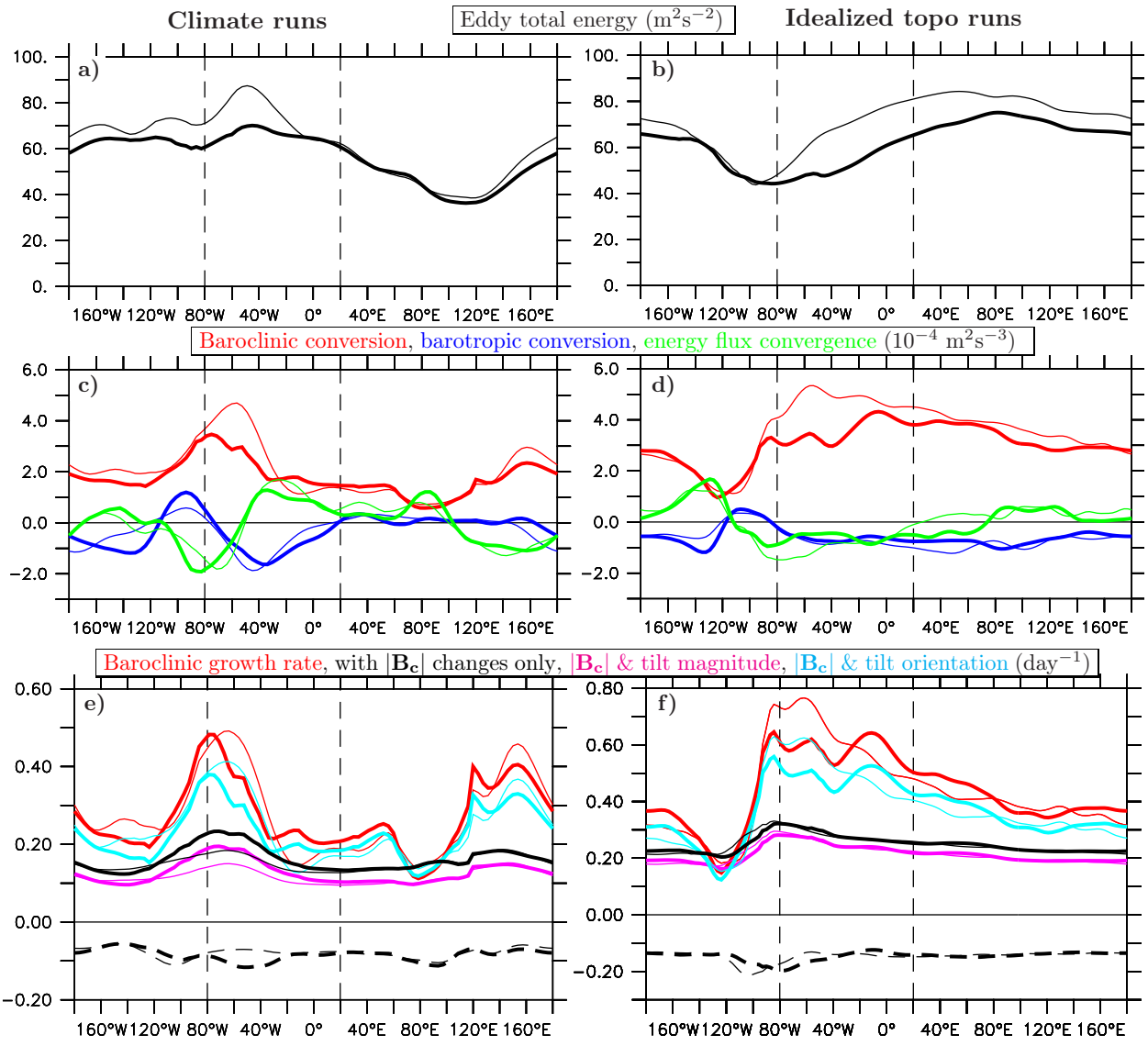

FIG. 3. ETE budget for (left column) the climate runs and (right column) the idealized topography runs where the thin and thick lines correspond to PI and LGM conditions respectively. (a), (b) ETE averaged between 250 and 850 hPa and between 25°N and 65°N. (c), (d) Baroclinic conversion (red), barotropic conversion (blue) and energy flux convergence (green). (e), (f) Baroclinic growth rate (red), with $|\mathbf{B_c}|$ changes only (black), both $|\mathbf{B_c}|$ and tilt magnitude changes (magenta) and both $|\mathbf{B_c}|$ and tilt orientation changes (cyan). All the quantities have been averaged between 250 and 850 hPa and between 25°N and 65°N. The dashed black lines correspond to the residual term, the third term on the rhs of Eq.(7). The vertical dashed lines indicate the North Atlantic sector between 80°W and 20°E.

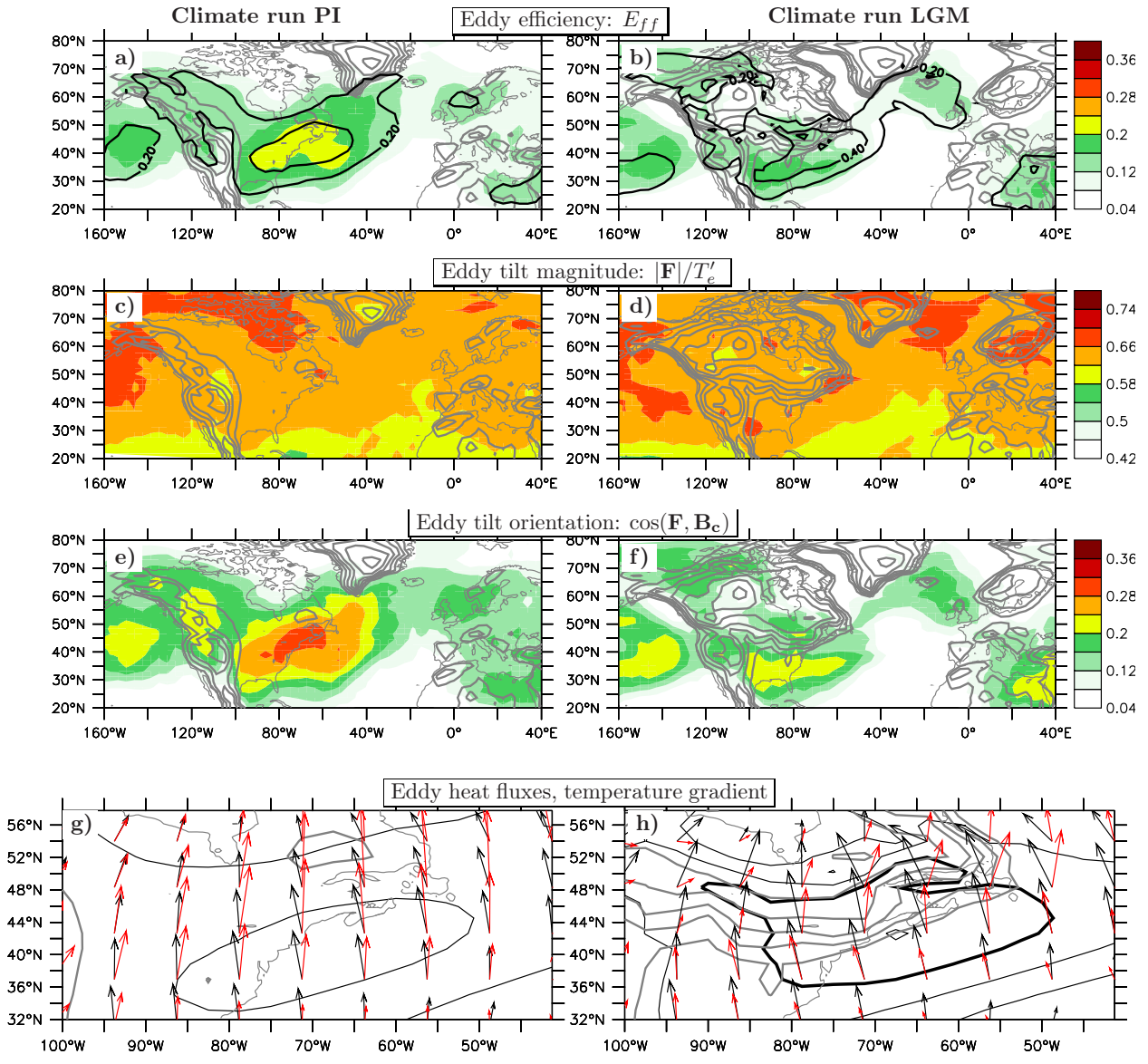

644 FIG. 4. Time mean and vertical average (250-850 hPa) of various quantities involved in the baroclinic conver-
645 sion term for (left) the PI climate run and (right) the LGM climate run: (a),(b) the baroclinic growth rate $|\mathbf{B_c}|E_{ff}$
646 (contours; int: 0.2 day^{-1}) and the eddy efficiency E_{ff} (shadings); (c),(d) the tilt magnitude $|\mathbf{F}|/T'_e$; (e), (f) the
647 tilt orientation $\cos(\mathbf{F}, \mathbf{B_c})$; (g), (h) the eddy heat fluxes (red) and minus the temperature gradient (black), and
648 Eady growth rate $0.31|\mathbf{B_c}|$ (contours; int 0.2 day^{-1} with 0.8 day^{-1} in thick contour). Grey contours correspond
649 to the height of the orography (int: 500 m, starting from 500m).

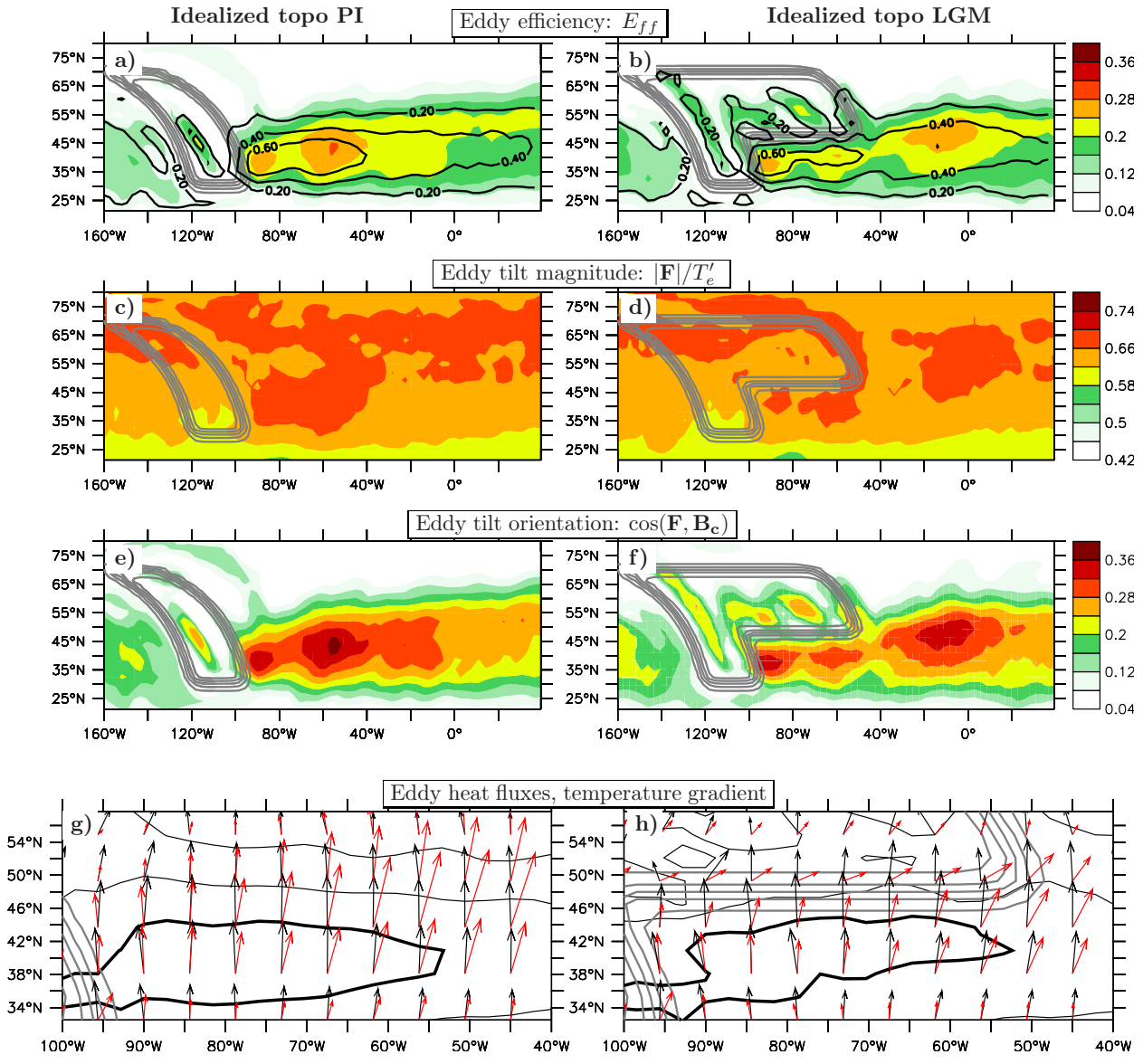

650 FIG. 5. As in Fig. 4 but for the simulations forced with (left) idealized Rockies (right) idealized LGM topog-
651 raphy.

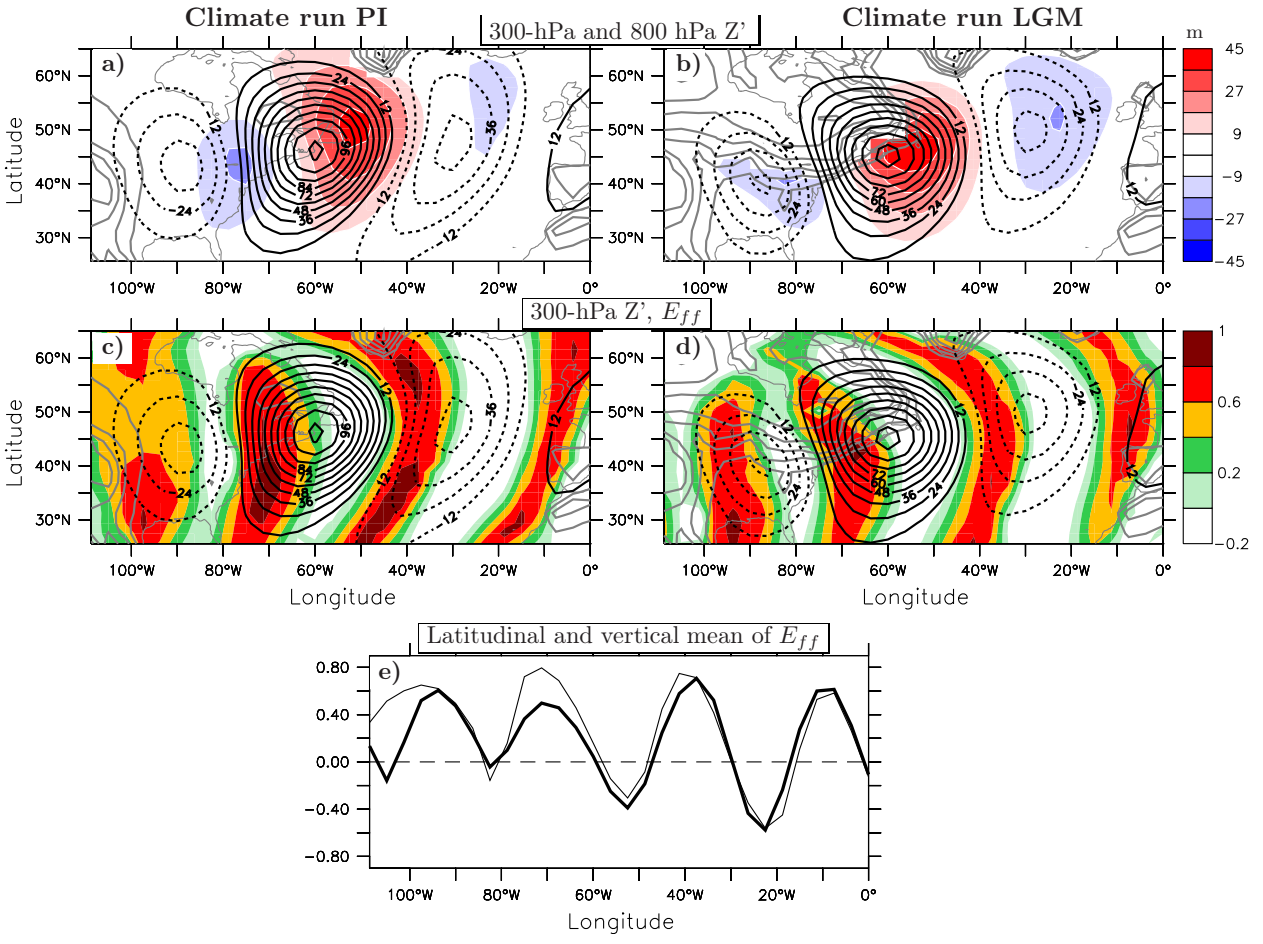

652 FIG. 6. One-point regression based on 300-hPa high-pass geopotential height Z' at 60°W, 45°N for (left) the PI
653 climate run and (right) the LGM climate run; (a), (b) 300-hPa Z' (contours; int: 12 m) and 800-hPa Z' (shadings;
654 int: 9 m); (c), (d) 300-hPa Z' (contours; int: 12 m) and associated vertically-averaged efficiency E_{ff} (shadings;
655 int: 0.05); (e) vertical and latitudinal average of the regressed efficiency E_{ff} for PI (thin line) and LGM (thick
656 line). In (a)-(d), grey contours correspond to the height of the orography (int: 500 m, starting from 500m).

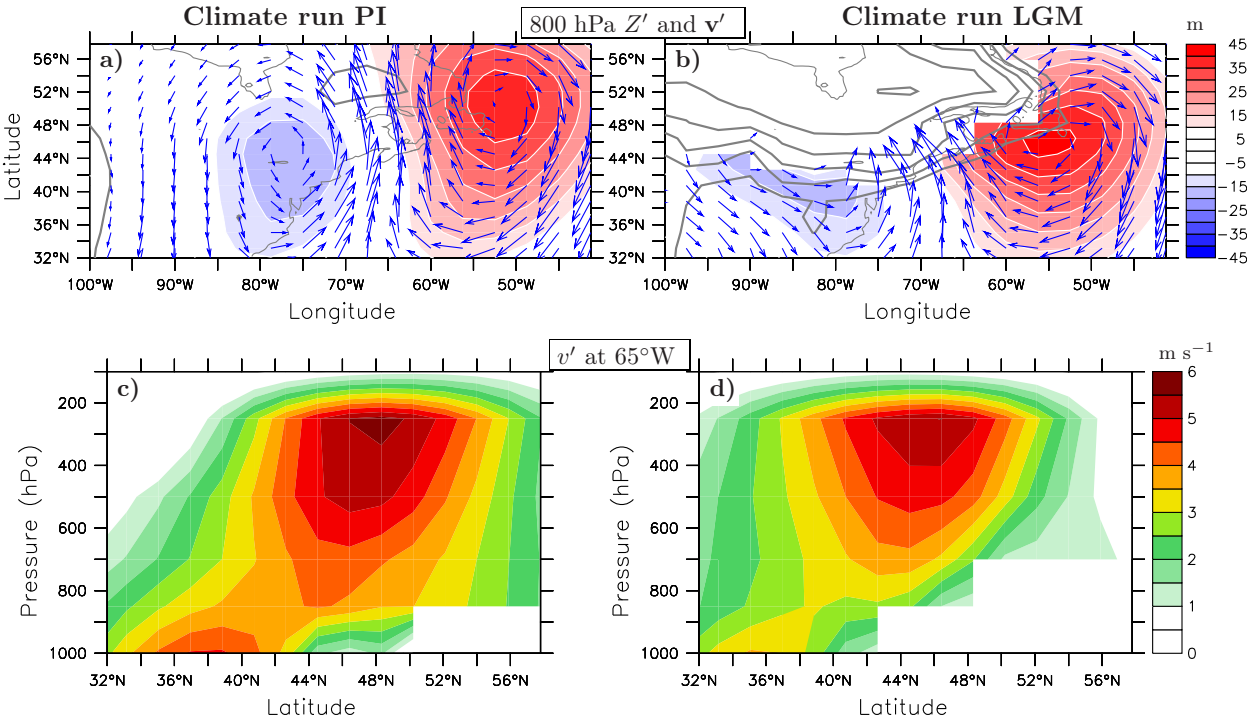

FIG. 7. Same regression as in Fig. 6 for (left) the PI climate run and (right) the LGM climate run. The regressed variables are (a), (b) the 800-hPa perturbation geopotential height Z' (shadings; int: 9 m) and wind $\mathbf{v}'$; (c), (d) perturbation meridional wind v' at 65°W (shadings). Grey contours correspond to the height of the orography (int: 500 m, starting from 500m).

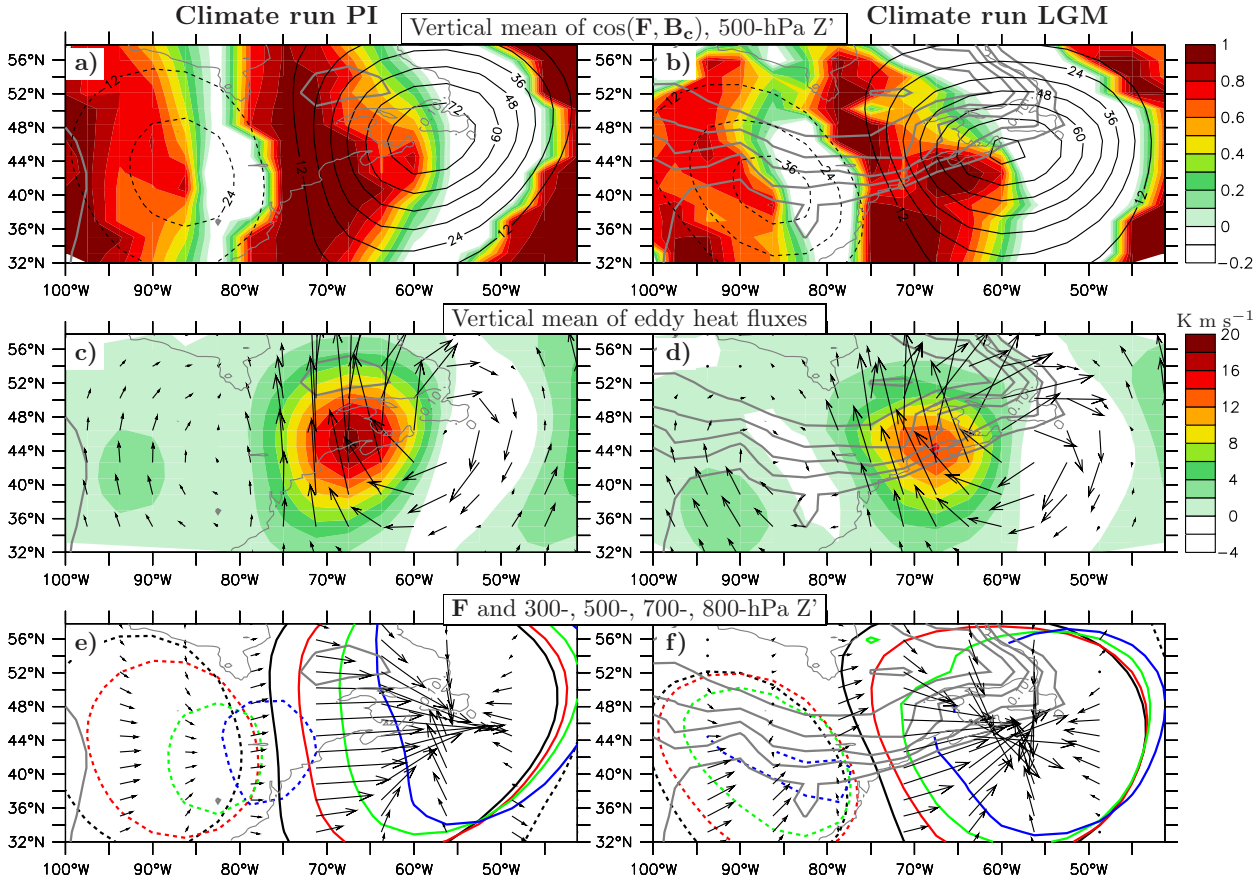

FIG. 8. Same regression as in Fig. 6 for (left) the PI climate run and (right) the LGM climate run. The regressed variables are (a), (b) the vertically-averaged tilt orientation $\cos(\mathbf{F}, \mathbf{B_c})$ (shadings) and 500-hPa perturbation geopotential height Z' (contours; int:12 m s^{-1}); (c), (d) the vertical averages of the heat fluxes (vectors) and their meridional component (shadings); (e), (f) the vertically-averaged $\mathbf{F}$ vector (arrows) and the 20-m contour of eddy geopotential height Z' at 300 (black), 500 (red), 700 (green), 850 hPa (blue). Grey contours correspond to the height of the orography (int: 500 m, starting from 500m).

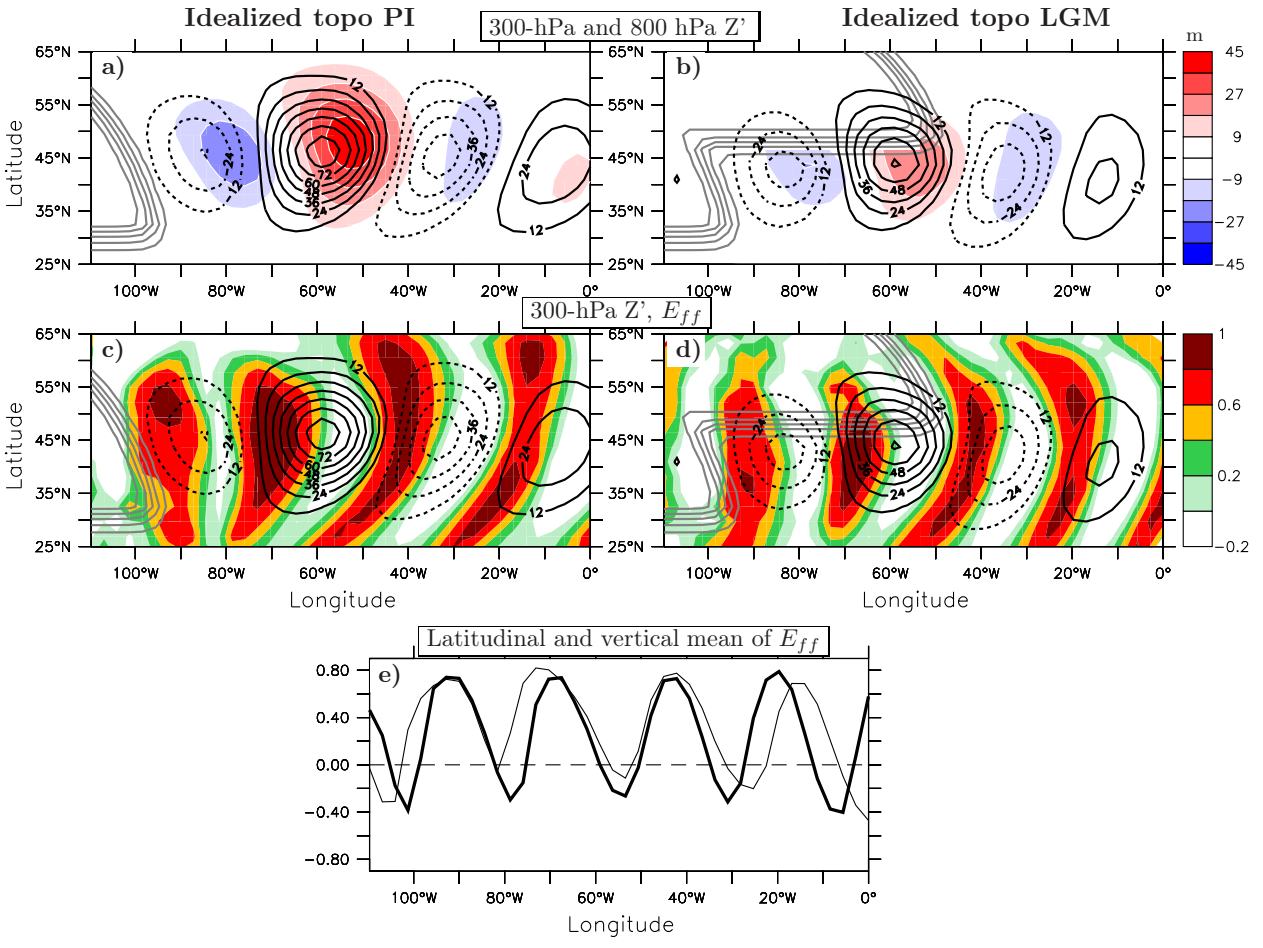

667 FIG. 9. As in Fig. 6 but for the simulations forced with (left) idealized Rockies (right) idealized LGM topog-
668 raphy.

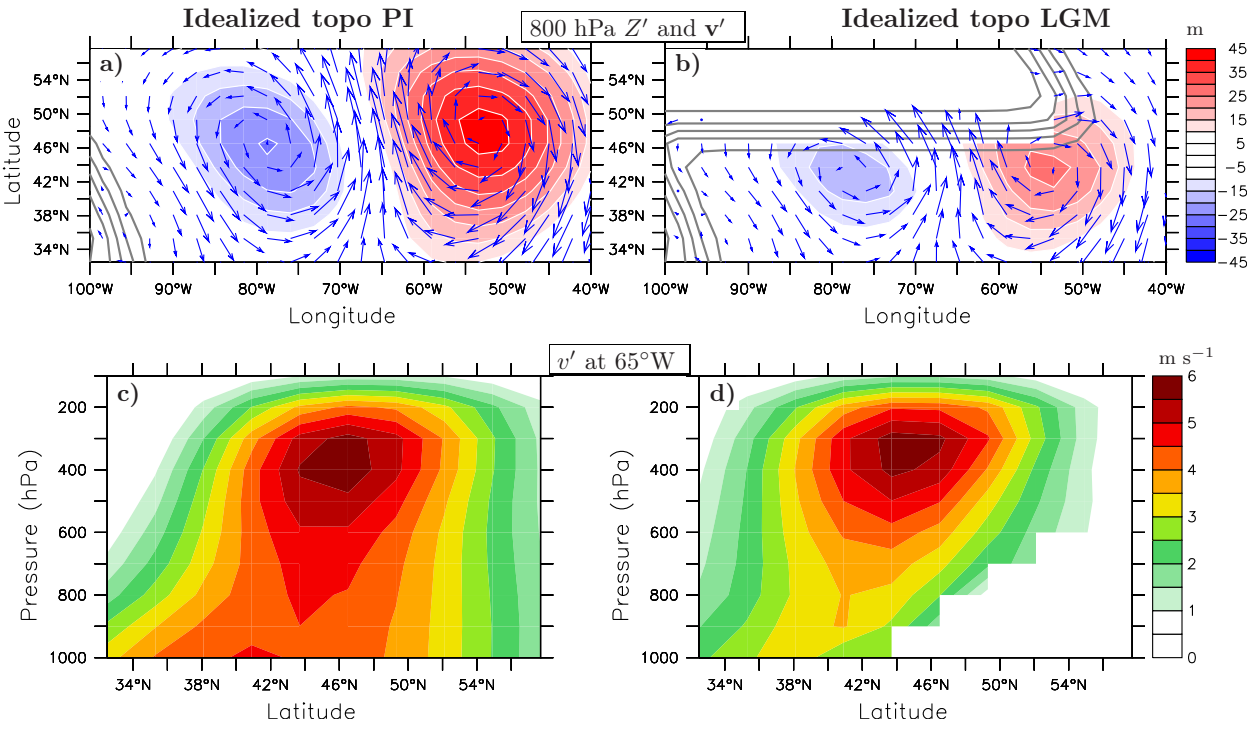

669 FIG. 10. As in Fig. 7 but for the simulations forced with (left) idealized Rockies (right) idealized LGM
670 topography.

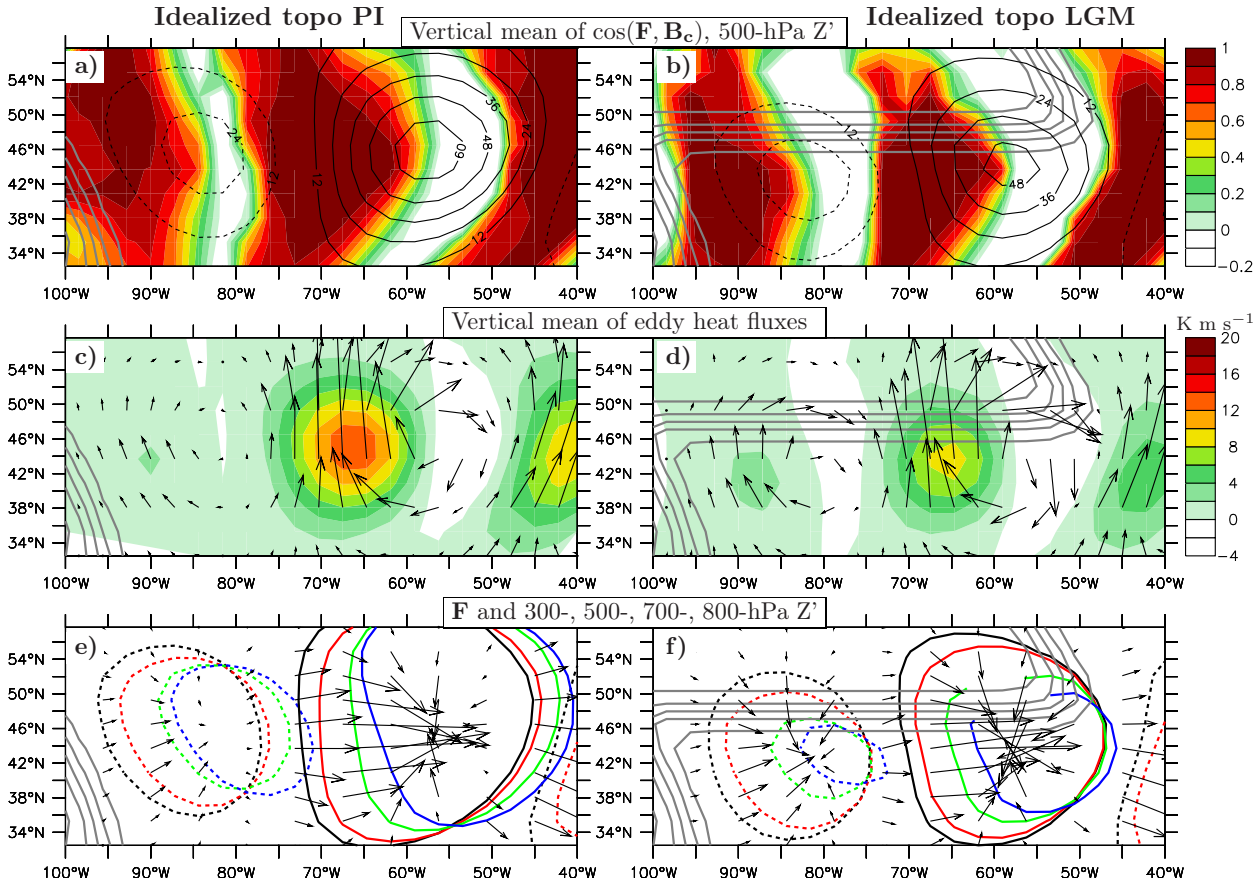

671 FIG. 11. As in Fig. 8 but for the simulations forced with (left) idealized Rockies (right) idealized LGM
672 topography.